Euler–Lagrange study of bubble drag reduction in turbulent channel flow and boundary layer flow Ⓕ

Xiaosong Zhang (张晓嵩), Jianhua Wang (王建华), and Decheng Wan (万德成) ⓘD

COLLECTIONS

Ⓕ This paper was selected as Featured

Euler–Lagrange study of bubble drag reduction in turbulent channel flow and boundary layer flow F SCI

Xiaosong Zhang (张晓嵩),[1,2] Jianhua Wang (王建华),[1] and Decheng Wan (万德成)[1,a] ID

AFFILIATIONS

[1] Computational Marine Hydrodynamics Lab (CMHL), State Key Laboratory of Ocean Engineering, School of Naval Architecture, Ocean and Civil Engineering, Shanghai Jiao Tong University, Shanghai 200240, China

[2] CSIC Shanghai Marine Energy Saving Technology Development Co., Ltd., No. 185 Gao Xiong Road, Shanghai, China

[a] Author to whom correspondence should be addressed: dcwan@sjtu.edu.cn. URL: http://dcwan.sjtu.edu.cn/.

ABSTRACT

The excellent drag reduction effect of the bubble drag reduction technique has been proved through many experiments since it was proposed. In this paper, the authors investigate the bubble-turbulence interaction and the corresponding drag reduction effect with a two-way coupled Euler–Lagrange code. The liquid phase is simulated by using a large eddy simulation method with the immersed bubbles treated using a nonlinear collision model to accurately simulate the bubble–wall interaction. A Gaussian distributed method is adopted to obtain the void fraction and interphase forces in the two-way coupled algorithm. Two typical wall-bounded turbulent flow problems (turbulent channel flow and boundary layer flow) are simulated to validate the accuracy and stability in bubbly flows and investigate the drag reduction mechanism. First, the effect of bubbles on the turbulent flow is studied in the channel flow cases in which the bubbles are observed attaching to the upper plate and swaying in the spanwise direction. In this case, Reynolds stress near the wall is decreased, which contributes to the drag reduction. Moreover, drag reduction of a turbulent boundary layer flow with bubble injection is studied in which the drag reduction under different air flow rates is in good agreement with experimental results. The contribution of turbulence and different liquid forces to the migration of bubbles away from the wall is investigated. The bubble trajectory in the turbulent boundary layer is divided into three distinct stages and discussed in detail finally.

Published under license by AIP Publishing. https://doi.org/10.1063/1.5141608

I. INTRODUCTION

Ship hull resistance is mainly composed of two aspects, the wave making resistance and the skin frictional resistance. It has been reported that skin frictional resistance accounts for as much as 60%–70% of the total drag for a cargo ship and about 80% of that for a tanker. Therefore, reducing frictional resistance is of great importance to save cost in the shipping industry in the marine transportation business.[1] Frictional drag reduction techniques can be divided into passive and active methods. Passive methods do not require extra energy consumption, such as the superhydrophobic surface coating technology[2–4] that is hot in recent years. Active methods require extra energy consumption, but the drag reduction effect can be better in general. The Bubble Drag Reduction (BDR) technique

is one of the most effective active methods. By delivering gas to the bottom of ships as discrete bubbles, BDR technology reduces the frictional resistance by changing the flow medium around the hull. The bottom of the ship hull is often simplified into a flat plate for the fundamental study of the bubby flow in the boundary layer.

Many experimental investigations have been performed to study the drag reduction effect of BDR technology. McCormick and Bhattacharyya[5] reported the earliest successful bubble drag reduction experiment with the Reynolds number around 1.8×10^6. Results showed that the drag reduction depends on the ratio of air mass flow. Madavan *et al.*[6,7] carried out experimental studies on the bubble drag reduction of a turbulent boundary layer. Pal *et al.*[8] performed a similar experiment and measured the trajectories of

bubbles. They found bubbles entering the boundary layer contribute to drag reduction. Thus, plenty of microbubbles immersed in the turbulent boundary layer are beneficial to lower the resistance. In the last few decades, a series of experiments[9–11] were carried out in the U.S. Navy's Large Cavitation Channel to investigate bubble drag reduction under different air flow rates and flow velocities, with the Reynolds number as high as 2.1×10^8. The drag reduction effect decreases gradually while going downstream. At the lowest test speed, the maximum drag reduction effect reaches 80% due to the formation of the air layer. More recently, Jacob et al.[12] studied the effect of bubbles on near-wall turbulent structures in a boundary layer flow experiment. Hassan and Morteza[13] showed that there is an optimal amount of air injection beyond which the drag reduction effect will be reduced. Park et al.[14,15] reported the void wave phenomenon discovered in the experiments and discussed the void wave frequency. These precisely designed experiments have demonstrated the drag reduction effect under a variety of conditions. Jiang et al.[16] carried out an experimental investigation on BDR characteristics of a vehicle. Significant drag reduction can be received when an air cavity is formed.

However, the experimental method failed in extracting the flow information about the entire domain. An alternative to overcome this is the numerical simulation. The Euler–Euler method is one of the most commonly used modeling methods, and both the continuous phase and discrete phase are governed by using the Navier–Stokes equations. The biggest advantage of this method is low computational burden so that it can be applied to the simulation of dense two-phase flow. Kunz et al.[17] developed an unstructured 3D two-fluid method code and simulated the high Reynolds number external bubble flows with qualitative and quantitative comparisons. Then, the code was improved and validated across a wide range of Reynolds numbers.[18] Mohanarangam et al.[19] combined the Computational Fluid Dynamics (CFD) method in the Euler framework with the Population Balance Model (PBM). Bubble coalescence and breakup were considered using the PBM method. The computational solutions fit well with the experimental results.[6] Xiang et al.[20] adopted a population balance approach based on the Multiple-Size-Group (MUSIG) model to simulate the dynamical effects of bubbly flow along a test body. Qin et al.[21] carried out both the experimental test and two-fluid simulation of bubble drag reduction on a flat plate. Detailed streamwise distribution of BDR is revealed in their study.

In order to resolve the detailed behavior of bubbles and investigate the underlying mechanism, many scholars have tried to adopt more refined numerical methods. Direct numerical simulation (DNS) of two-phase flow is undoubtedly the most refined method in which both bubbles and turbulence are directly solved. However, the huge computational cost hinders the application of this method. Recently, Lakehal et al.[22] performed DNS simulations of turbulent channel flow laden with microbubbles. Despite the use of a block mesh refinement technique, calculation with 30×10^6 grids only simulated 600 bubbles. Therefore, the Euler–Lagrange method is more popular in the study of interaction between a large amount of bubbles and turbulent flow. In this method, the liquid phase is governed using N–S equations and each bubble is tracked individually using the kinematic equation in the Lagrange framework. Xu et al.[23] performed the earliest numerical simulation of bubble drag reduction in a channel flow. The fluid was solved by using the Direct Numerical Simulation (DNS) method and bubbles were captured by using the Lagrange method. The results showed that relatively smaller spherical bubbles will produce a sustained level of drag reduction over time. The same method is used by Ferrante and Elghobashi[24] to investigate the underlying mechanism responsible for drag reduction in a bubble-laden turbulent boundary layer over a flat plate. A local positive divergence of the fluid velocity was found in the presence of bubbles. Mattson and Mahesh[25] studied the bubble migration in the turbulent boundary and derived an excellent guidance for the application of bubble drag reduction technology. Pang et al.[26] developed a two-way coupled Euler–Lagrange code combined with the DNS method and simulated the bubble distribution in a vertical channel flow. The effect of gravity on bubble distribution was considered in their paper. Simultaneously, Molin et al.[27] simulated the bubbly vertical channel flow. They focused on the effects of bubbles on turbulence. More recently, Pang et al.[28] adopted their code to study the interaction between bubbles and liquid turbulence with the help of interphase forces in a horizontal channel flow. The Reynolds number in their simulation is $Re_\tau = 150$. Asiagbe et al.[29] also carried out the channel flow simulation with bubbles. Specifically, they adopted the Large Eddy Simulation (LES) model to simulate the liquid phase. LES simulation can resolve the velocity fluctuations reasonably with less computational resources in contrast with the DNS method. The use of the LES method makes it possible to carry out the simulation of higher Reynolds numbers.

Summing up the above mechanism using the Euler–Lagrange method, numerical methods in previous studies were often highly simplified. First, the bubble–bubble interaction and bubble–wall interaction were used to be ignored[28] or modeled by using the simple hard sphere model to describe collision.[25,29] These simplifications do not correctly describe the movement of bubbles near the wall surface and affect the calculated drag reduction effect. Second, in most of the previous two-way coupled simulations, the effect of bubbles on the fluid is only presented by a coupled source term. In fact, the volume fraction in which bubbles occupy a portion of the fluid volume also plays an important role in the drag reduction effect calculation. The traditional two-way coupling algorithm fails when the bubble diameter is larger than the grid scale because of the problem in calculating the volume fraction. In this paper, a more realistic nonlinear model is adopted to solve elastic collision. The void fraction effect is considered in the liquid phase governing equations, and a Gaussian distributed method is adopted to perform a more accurate two-phase coupling algorithm. Turbulent channel flow and turbulent boundary layer flow are two most typical fluid conditions. Both of them are the classic problems of wall-bounded turbulence investigation, and they are similar to how bubble drag reduction works. Therefore, these two problems are simulated to validate the accuracy and stability in bubbly flows and investigate the drag reduction mechanism.

This paper is organized as follows: First, the mathematical method is introduced in detail, including the liquid phase solving, bubble motion tracking, and the two-way coupling algorithm. Then, two foundational cases are set to validate the accuracy of the hydrodynamic model and collision force model. The computational results and the bubbly channel flow are shown in Sec. IV, and the bubbly turbulent boundary layer flow is presented in Sec. V. Finally, conclusions are provided.

II. MATHEMATICAL MODELING

In the Euler–Lagrange method, the continuous phase (liquid) and discrete phase (bubble) are solved in different frameworks. In this paper, the liquid phase is solved using the LES method in the Euler framework, while bubbles are tracked using the kinematic equation following Newton's second law. The mathematical models for different phase calculations and coupling are introduced in detail as follows.

A. Liquid phase solving

In order to consider both flow field details and computational costs, the LES method is adopted to solve the turbulence liquid phase. The eddy in the flow field is filtered according to the scale. The large-scale vortex structure is directly solved, while the small-scale one is approximated using the sub-grid model. The filtered continuity and momentum equations are written as

$$\frac{\partial \alpha}{\partial t} + \frac{\partial \alpha \overline{u_i}}{\partial x_i} = 0, \tag{1}$$

$$\frac{\partial \alpha \overline{u_i}}{\partial t} + \overline{u_j}\frac{\partial \alpha \overline{u_i}}{\partial x_j} = -\frac{1}{\rho}\frac{\partial \overline{p}}{\partial x_i} - \frac{\partial}{\partial x_j}(\overline{\sigma_{ij}} + \tau_{ij}) + \alpha g + S_u + \frac{f_{pf}}{\rho}, \tag{2}$$

where the overbar identifies filtered quantities, u_i is the fluid velocity in three directions ($i = x$, y, and z), α is the fluid volume fraction, ρ is the fluid density, p is the pressure, σ_{ij} is the viscous stress, and S_u represents the pressure gradient source term, which is only required in the channel flow simulation. The last term is the coupled source term, which reflects the effect of bubbles on the fluid. The sub-grid scale stress tensor τ_{ij}, which is required to close Eqs. (1) and (2), is given by

$$\tau_{ij} = \overline{u_i}\,\overline{u_j} - \overline{u_i u_j}. \tag{3}$$

The SGS stress is modeled using the Wall Adapting Local Eddy (WALE)-viscosity model.[30] The turbulent kinematic eddy-viscosity is defined as

$$\nu_t = (C_w \Delta)^2 \frac{\left(S_{ij}^d S_{ij}^d\right)^{3/2}}{\left(\overline{S}_{ij}\overline{S}_{ij}\right)^{5/2} + \left(S_{ij}^d S_{ij}^d\right)^{5/4}}, \tag{4}$$

where the filter width Δ is calculated by $\Delta = V^{1/3}$. C_w is a constant number, which is set to be 0.325 in the present study. S_{ij} is the strain-rate tensor, which satisfies

$$S_{ij}^d = \frac{1}{2}\left(\overline{g}_{ij}^2 + \overline{g}_{ji}^2\right) - \frac{1}{3}\delta_{ij}\overline{g}_{kk}^2, \quad \overline{g}_{ij} = \frac{\partial \overline{u_i}}{\partial x_j}. \tag{5}$$

B. Lagrange tracking of bubble motion

The motion of bubbles in a carrier flow field can be described using the kinematic equation following Newton's second law. Bubbles are assumed to be non-deformable spheres with a constant diameter in this study. With the tiny bubble–liquid density ratio, bubbles are subjected to drag force, lift force, gravity, buoyancy, and fluid acceleration force. Each bubble is tracked individually by solving the equation as follows:

$$m\frac{dv}{dt} = f_D + f_L + f_P + f_G + f_C$$

$$= \frac{3mC_D}{4d}|u - v|(u - v) + \frac{m\rho_l}{\rho_b}C_L(u - v) \times (\nabla \times u)$$

$$+ \frac{m\rho_l}{\rho_b}\frac{Du}{Dt} + mg\left(1 - \frac{\rho_l}{\rho_b}\right) + f_C, \tag{6}$$

where v represents the bubble velocity, m is the mass of the bubble, d is the bubble diameter, and ρ_l and ρ_b represent the liquid density and bubble density, respectively. The terms on the right side of Eq. (6) represent the drag force, shear lift force, fluid acceleration force, gravity-buoyancy, and collision force, respectively. The drag force coefficient C_D and lift force coefficient C_L are determined by Tomiyama's drag model[31] and lift model[32] as follows:

$$C_D = \max\left(\min\left(\frac{16}{Re}(1 + 0.15Re^{0.687}), \frac{48}{Re}\right), \frac{8}{3}\frac{Eo}{Eo + 4}\right), \tag{7}$$

$$C_L = \begin{cases} \min[0.288\tanh(0.121\,Re), f(Eo_d)], & Eo_d < 4 \\ f(Eo_d), & 4 \le Eo_d \le 10.7, \end{cases}$$

$$f(Eo_d) = 0.001\,05Eo_d^3 - 0.0159Eo_d^2 - 0.0204Eo_d + 0.474, \tag{8}$$

where the bubble Reynolds number is defined as $Re = d|u - v|/\nu$, Eotvos number Eo is defined as $Eo = g|\rho_l - \rho_b|/\sigma$, σ is the surface tension coefficient, which is 0.072 in the present study. The drag model and lift model have been proved to be accurate enough under the Reynolds number and bubble size studied in this paper.

The last term of Eq. (6) is the collision force. Previous studies usually ignored the interaction between bubbles[28] or used the hard sphere model to simulate the collision.[25,29] However, the collision between bubbles and the wall always exists in the problem of bubble drag reduction. The bubble–wall collision affects how well the bubbles adhere to the wall, resulting in obvious influence on the drag reduction effect. Some studies have been performed to analyze the interaction between bubbles and the wall,[33] and some practical models have been proposed. In this paper, a non-linear collision force model proposed by Heitkam et al.[34] is adopted to describe the bubble–bubble interaction and bubble–wall interaction. The elastic and viscous contact forces can be obtained by

$$F_{elastic} = 18.5\sigma\left(\frac{\Delta}{R_{eq}}\right)^2 + 2.0\Delta\sigma, \tag{9}$$

$$F_{viscous} = uC_{bc}\frac{12\mu_l}{2\pi}0.34\left(\frac{\Delta}{R_{eq}} + 0.0002\right)^{-0.5}$$

$$\times \left(4.0\sqrt{\frac{R_{eq}^3}{h_0}} + 3.0R_a\frac{R_{eq}}{h_0}\right), \tag{10}$$

where R_{eq} is the effective radius, Δ is the deformation of the bubble, h_0 is the gap width when the bubble approaches another bubble or a wall. The parameter C_{bc} represents the collision partner, which is equal to 1 for bubble–wall collision and 0.25 for bubble–bubble collision.

C. Two-phase coupling

The two-way coupled solving algorithm between the Euler liquid phase and Lagrange bubble phase is achieved by the following steps:

- Calculate the hydrodynamic and collision forces on the bubbles.
- Solve Eq. (6) and update the bubble locations.
- The local void fraction of the liquid is calculated according to the position of the bubble in the liquid.
- The hydrodynamic forces acting on the bubble are applied to the liquid as source terms according to Newton's third law.
- Solve the liquid governing equations.

The key problem of this solving algorithm is the calculation of void fraction distribution and coupled forces distribution from the instantaneous bubble sizes and locations. Initially, the void fraction was defined in each computational cell as the ratio of the total volume of bubbles in the cell by the cell volume.[35] However, this was found not totally satisfactory because of the non-continuous character of the void fraction across cells.[36] Boundary layer grids are usually thin in the case of resistance calculation. When the grid height is less than the diameter of the bubble, the void fraction caused by the bubble and its effect on the fluid are all calculated in the grid where its mass center is located, although a large part of its volume is outside the grid. This wrong condition can be seen in Fig. 2(a).

In order to improve the authenticity and stability of the code, a Gaussian bubble volume distribution scheme as in Refs. 35 and 37 is adopted to smooth the bubble volume into the grid it should be in.

With the help of Fig. 1, the computation scheme is explained as follows. There is a bubble j in the field, and the green box represents its "affected region." The contribution of bubble j to the volume fraction of the grid cell k in the affected region can be obtained by averaging the bubble volume into the grid. The expression is

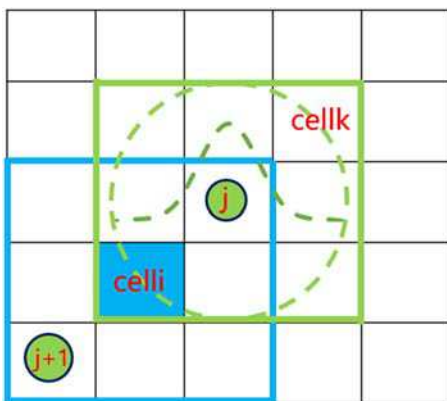$$\alpha_k = \frac{V_j^b}{\sum_k^{Ncells} V_k^{cell}}, \quad (11)$$

where V_j^b and V_k^{cell} represent the volumes of bubble j and cell k, respectively. N_{cells} is the number of cells in the affected region of bubble j. In fact, the shape of bubbles cannot be represented by uniform distribution. Larger contribution should be received for the cells near the bubble center. Thus, the expression (11) is modified by multiplying by a Gaussian weight function,

$$\alpha_k = \frac{V_j^b}{\sum_k^{N_{cells}} V_k^{cell}} f_{k,j}, \quad f_{k,j} = \frac{1}{\sqrt{2\pi}S} e^{-\left(|x_{kj}|^2 / 2S^2\right)}, \quad (12)$$

where $|x_{kj}|$ represents the distance between cell k and bubble j and S is the standard deviation. It is worth noting that a one-dimensional Gaussian distribution is used in the present work as function (12). This is because bubbles can only be higher than the grid size in the wall-normal direction, so the bubble volume only needs to be smoothed in this direction. Applying Gaussian distribution to the affected region is equivalent to cutting off the range, which will ignore part of the bubble volume. In order to keep the mass conservation, the α_k needs to be multiplied by a normalization factor, which is defined as the ratio of the original bubble volume to the distributed total bubble volume,

$$W_k = \frac{V_j^b}{\sum_k^{N_{cells}} (V_k^{cell} \alpha_k)} = \frac{V_j^b}{\sum_k^{cell} \left(V_k^{cell} \frac{V_j^b}{\sum_k^{Ncells} V_k^{cell}} f_{k,j} \right)} = \frac{\sum_k^{N_{cells}} V_k^{cell}}{\sum_k^{N_{cells}} (V_k^{cell} f_{k,j})}. \quad (13)$$

By multiplying by the factor W_k, the α_k can be expressed as

$$\alpha_k = \frac{V_j^b}{\sum_k^{Ncells} (V_k^{cell} f_{k,j})} f_{k,j}. \quad (14)$$

For cell i in Fig. 1, the void fraction is obtained by adding up the effect of all bubbles in the affected region,

FIG. 1. Illustration of the void fraction computation using the Gaussian distribution scheme.
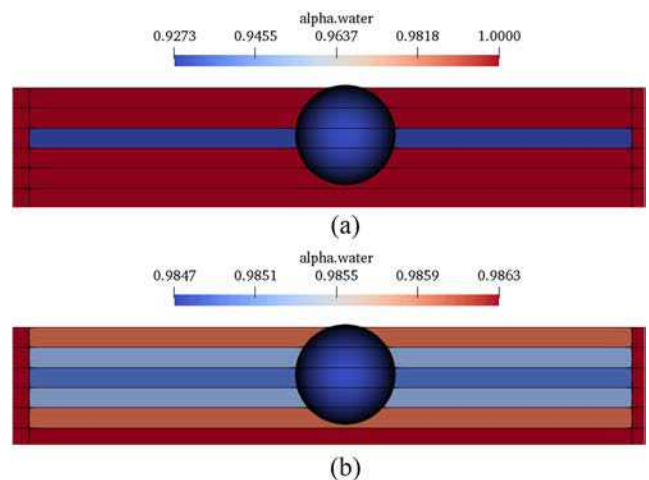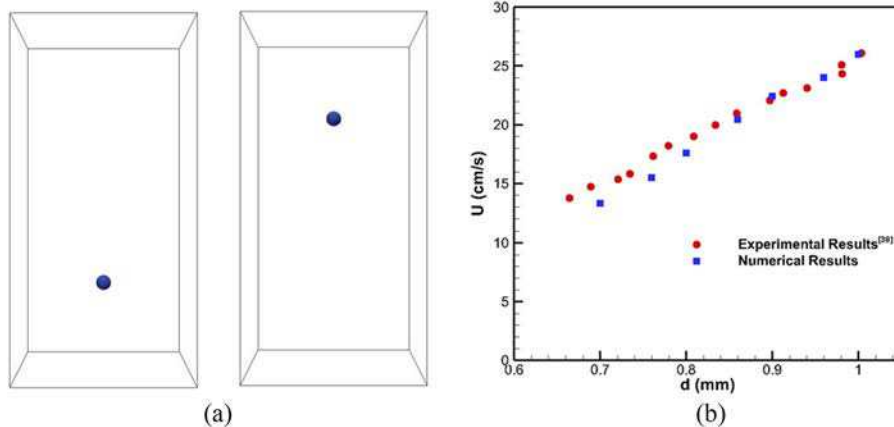

FIG. 2. Void fraction computation when a single bubble is close to the wall. (a) Traditional volume fraction calculation without the distributed algorithm. (b) Volume fraction calculation with the distributed algorithm.

FIG. 3. The rising bubble simulation and velocity comparison with the experiment. (a) Numerical simulation of a rising bubble in calm water. (b) Rising velocity comparison of bubbles with different diameters.

$$\alpha_i = \sum_{j=1}^{N_i} \frac{f_{k,j} V_j^b}{\sum\limits_{k}^{Ncells} \left(V_k^{cell} f_{k,j} \right)}. \tag{15}$$

Figure 2 shows the void fraction calculation with and without distribution function. By using this two-way coupled solving algorithm, the authenticity and robustness of the program have been significantly improved.

III. MODEL VALIDATION

The bubble kinematic equation (6) includes several source terms. These source terms can be divided into two types: hydrodynamic forces on bubbles and collision force on bubbles. Both of them are calculated using some models. In this section, two foundational cases are set to validate the accuracy of the hydrodynamic model and collision force model.

First, the rising velocity of bubbles in calm water is calculated. The forces acting on the bubble as it rises are balanced, and the bubble eventually reaches a constant velocity. The velocity is validated by comparison with the experimental results of Duineveld.[38]

Simulations with different bubble diameters are carried out. The rising velocities of bubbles are in good agreement with the

experimental results as shown in Fig. 3, which proves the accuracy of the computational hydrodynamic force on the bubbles.

Next, the accuracy of the collision force calculation is validated by the trajectory and deformation of a single bubble in collision with a plate. Heitkam et al.[34] designed an experiment in which small bubbles collide with a flat plate in an oblique way. The process of bubble rise, collision, deformation, and sliding was all included in the experiment. All of them are the main behaviors of bubble dynamics in drag reduction problems. Thus, this experiment is chosen for comparison. The bubble movement process is shown in Fig. 4.

Many discrete points are obtained by repeated experiments of multiple bubbles. The bubble trajectories and deformations obtained by simulation are basically consistent with the trend of test points, which proves the accuracy of calculating the bubble–wall interaction.

IV. BUBBLY CHANNEL FLOW SIMULATION

In this section, turbulent channel flow laden with bubbles is simulated to study the effect of bubbles on the turbulence. A fully developed single phase turbulent channel flow is simulated first, and
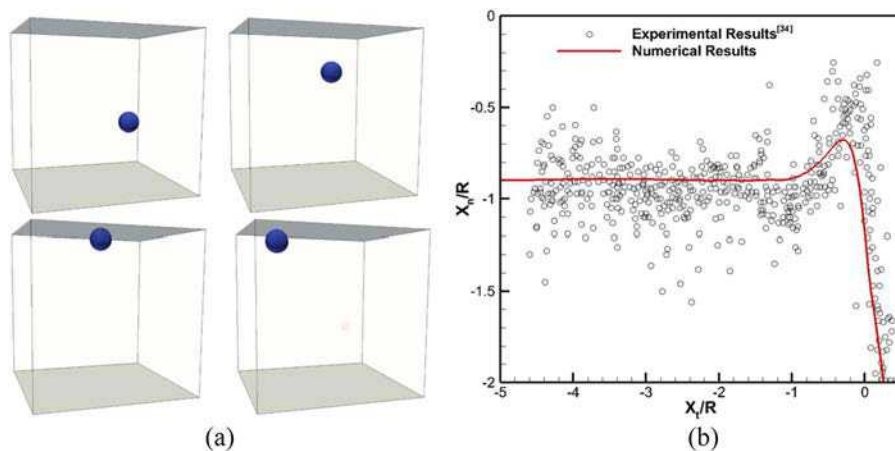
FIG. 4. Simulation of inclined bubble collision and trajectory comparison with the experiment. (a) Numerical simulation of inclined collision between a rising bubble and a plate. (b) Bubble trajectory comparison between numerical results and experimental data.
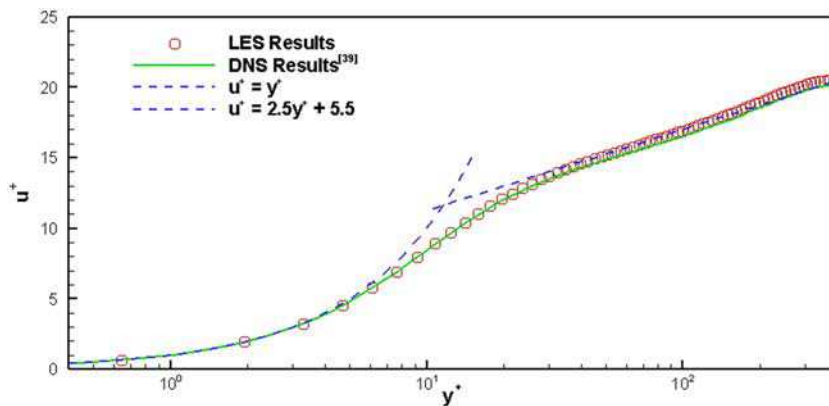
FIG. 5. Single phase mean streamwise velocity profile.

the turbulent characteristics are validated by comparison with DNS results of Moser *et al.*[39] On this basis, turbulent bubbly flow is simulated, and the influence of bubbles on mean velocity profile and Reynolds stress tensor is discussed.

A. Computational conditions and single phase simulation

Computational domain of the channel is a box domain whose size is $4h \times 2h \times 2h$. The half height of the channel is set to be 0.025 m, and the bulk velocity U_b is equal to 0.276 m/s. As a consequence, the value of $Re_b = 2hU_b/v = 13\,350$ is chosen to be corresponding to the target value of $Re_\tau = 395$. Structured grids are adopted for the spatial discretization. The computational domain is discretized using $N_x \times N_y \times N_z = 181 \times 181 \times 128$ grid points in three directions. The grids along the streamwise and spanwise directions are distributed uniformly and the large gradient is applied to the grids in the wall-normal direction to increase the resolution of the turbulent structures.

In order to simulate the fully developed turbulent flow, two pairs of periodic boundary conditions are adopted in the streamwise direction and spanwise direction. At the same time, the periodic boundary conditions are also applied to the bubble phase solving so that the void fraction in the channel will remain the same. The remaining two boundaries represent walls. For the liquid phase,

the no-slip boundary condition is applied to the walls, while for the bubble phase, the collision boundary condition is used. The bubble diameter is 110 μm, and the density is set to 1.2 kg/m^3. The total number of bubbles in the channel is 39 366, and correspondingly, the void fraction is $\alpha_b = 1.12 \times 10^{-4}$. This void fraction has been proved to be large enough to affect the turbulence field.[23,24]

At first, a single phase turbulent channel flow is simulated. The simulation is initialized by the uniform flow field and runs for a long time to ensure the removal of all transients related to initial conditions. Next, statistics in $t^+ = tu_\tau^2/v = 5000$ units of time are sampled and averaged for analysis. The accuracy of single phase turbulence results is validated by comparison with DNS results of Moser *et al.*[39] For the global flow quantities, the most important one is the computed average friction velocity, equivalently, the Reynolds number Re_τ based on the velocity. The computed Re_τ is equal to 375, which is under-predicted to the target value slightly. The error is acceptable for LES simulation. In the following results, the values are scaled with the computed friction velocity.

Figure 5 presents the steady mean streamwise velocity profile. The LES results fit well with the DNS results in the viscous sub-layer and buffer region. In the log-law region, slight over-prediction can be seen in contrast with the DNS results, but the difference is very small. Figure 6 shows the comparison of turbulent intensities and Reynolds stress. The LES results show good agreement with the DNS
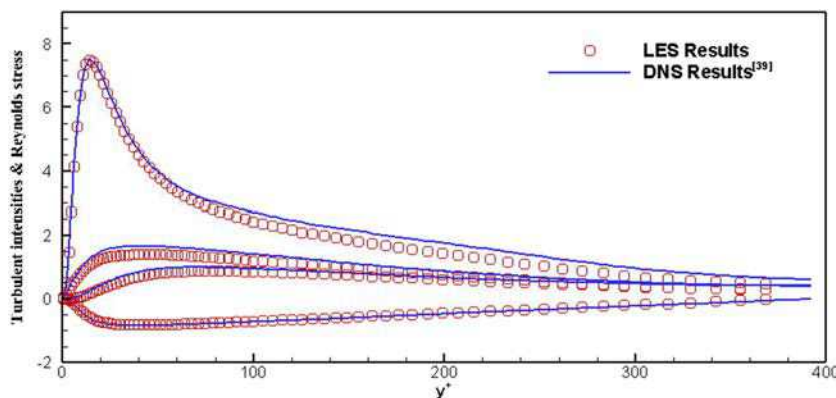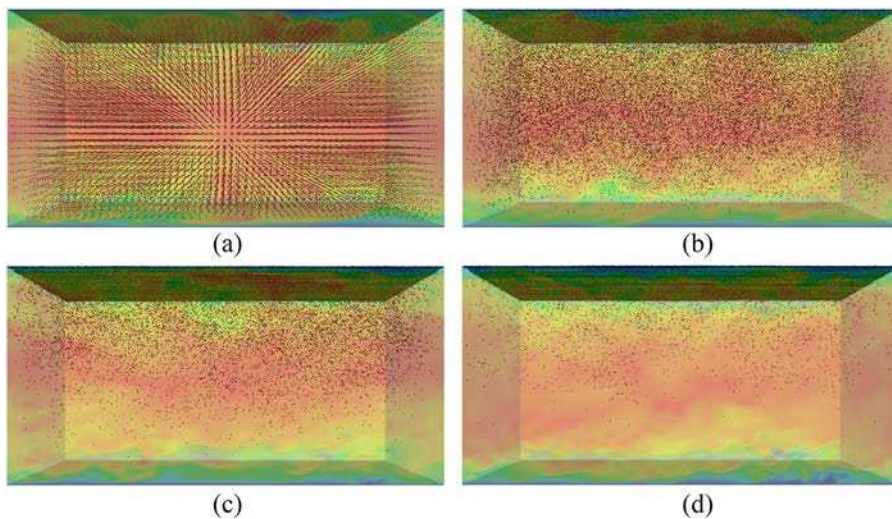

FIG. 6. Single phase turbulent intensities and Reynolds stress.

FIG. 7. Four typical moments in bubble evolution. (a) $t^+ = 0$. (b) $t^+ = 450$. (c) $t^+ = 1125$. (d) $t^+ = 1800$.

results, and the peak of velocity fluctuations can be basically captured. The single phase simulation and comparison confirm that the numerical method in the present work can well resolve the turbulent characteristics in the flow.

B. Channel flow laden with bubbles

After the fully developed turbulent channel flow is obtained, bubbles are injected into the channel uniformly. Figure 7 presents the evolution of bubbles in the channel. After the bubbles are injected into the flow field, they are affected by turbulence and become chaotic immediately. Buoyancy force is the dominant force in the wall-normal direction. Due to the large density difference, bubbles gradually migrate toward the upper wall of the channel. At $t^+ = 1800$, most of bubbles cling to the upper plate and move slowly along the downstream direction. However, as shown in Fig. 7(d), not all the bubbles are sticking to the upper wall after the flow field reaches stability. The lift force and fluid acceleration force acting on the bubbles force them to oscillate in the flow field.

Bubble distribution on the upper wall is shown in Fig. 8. It can be seen clearly that the bubbles are concentrated into filament-like structures. This phenomenon has also been observed in the previous experiment[15] and numerical simulations.[25] In the turbulent flow near a wall, vortex structures that form the legs of hairpin structures are oriented in the streamwise direction.[40] Thus, bubbles are attracted together by the downstream vortex structure and form

filament-like stripes. Except for the streamwise feature, the authors note that the bubble stripes sway continuously in the spanwise direction. The concentration of bubbles near the wall affects the turbulent characteristics of the flow field. Next, the influence of bubbles on the turbulent field is discussed by the comparison between the single-phase and the two-way coupled fluid mean velocity profiles and turbulent stresses.

The drag reduction effect is shown in Fig. 9. C_{f0} represents the averaged frictional resistance coefficients without bubble injection. As the bubbles gradually rise near the upper plate, drag reduction is becoming more and more obvious. Finally, about 7.1% drag reduction effect is obtained in the steady state. The drag reduction effect comes from two aspects. The first reason is that bubbles attached to the plate reduce the local fluid density. A decrease in fluid viscosity results in a decrease in frictional resistance. Another reason is that bubbles affect the turbulent flow structure. Bubbles near the plate reduce the energy of turbulence, which contributes to the turbulent drag reduction. Next, the modulation of bubbles on the liquid phase turbulence is analyzed in detail by the comparison of the mean velocity profile, turbulent intensities, and Reynolds stress.

Figure 10 shows the comparison of mean liquid velocity profiles with and without bubbles. The most obvious difference is that the velocity profile of the liquid containing bubbles presents an asymmetric shape in the channel. In the lower part of the channel, there is no change in the velocity profile because there are
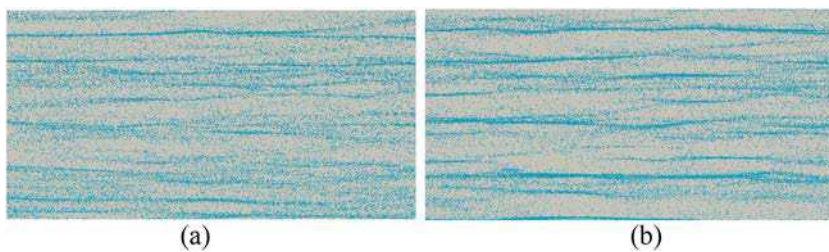
FIG. 8. Bubble distribution on the upper wall of the channel. (a) $t^+ = 1900$. (b) $t^+ = 2000$.
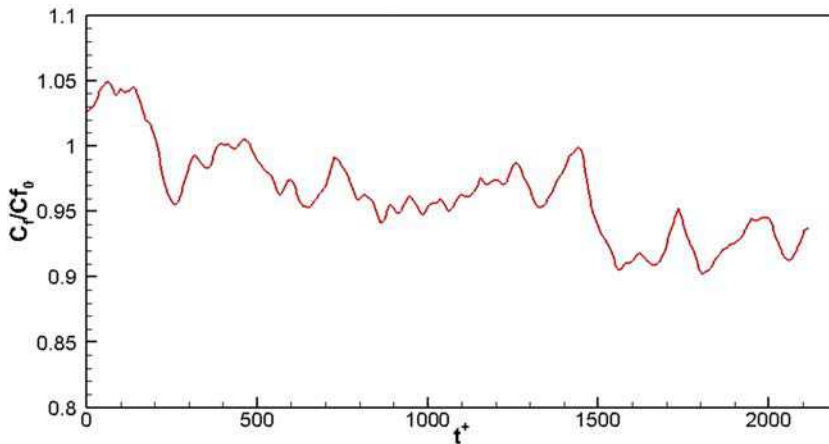
FIG. 9. Drag reduction effect of the upper wall after bubble injection.

no bubbles in this part. In the upper part of the channel, bubbles gather near the upper wall, which leads to a squeeze on the fluid away from the wall. As a consequence, there is a decrease in velocity at the region $y^+ > 600$, and velocity near the middle of channel is slightly higher than that in the pure liquid condition. This phenomenon is relatively similar to the simulation results of turbulent channel flow with solid particles.[41,42] As is known to all, the velocity gradient in the viscous sub-layer plays an important role in the frictional resistance. Figure 10 also shows the local velocity in the viscous sub-layer of the upper wall. Liquid velocity and its gradient decrease with the presence of bubbles, which contributes to drag reduction.

Figure 11 presents the turbulent intensities and Reynolds stress in the upper half of the channel with and without bubbles. The results in the lower half of the channel are not shown in the figure because the change is too small. First, the turbulent intensities decrease in all three directions: especially, the decrease is more obvious in the spanwise and wall-normal direction. As discussed above about the bubble distribution, bubbles in space oscillate in the wall-normal direction near the plate and bubble stripes on the plate sway in the spanwise direction. The authors believe that the bubble movement inhibits the turbulent vortex energy in the corresponding direction. At the same time, Reynolds stress decreases obviously with the impact of bubbles. According to the theoretical analysis of Fukagata et al.,[43] the frictional resistance coefficient of fully developed turbulent channel flow can be decomposed as Eq. (16). The two terms represent the laminar part and turbulent part, respectively. It can be seen that the decrease in Reynolds stress plays an important role in drag reduction. In other words, bubbles can reduce the turbulent drag by changing the Reynolds stress,

$$C_f = \frac{12}{\mathrm{Re}_b} + 12 \int_0^1 2(1-y)(-\overline{u'v'})dy. \qquad (16)$$

The near-wall turbulent vortex structure is considered to be directly related to the wall frictional resistance. In order to investigate the effect of bubbles on the vortex structure more intuitively, iso-surfaces of Q are plotted in Fig. 12. It can be obviously seen that the vortex structures are sparser in the upper half part of the channel than that in the lower half part of the channel. The local view of the figure shows the bubbles mixed in the turbulent vortex structure. It is these bubbles that reduce the development of the turbulent vortex, which contributes to the drag reduction.
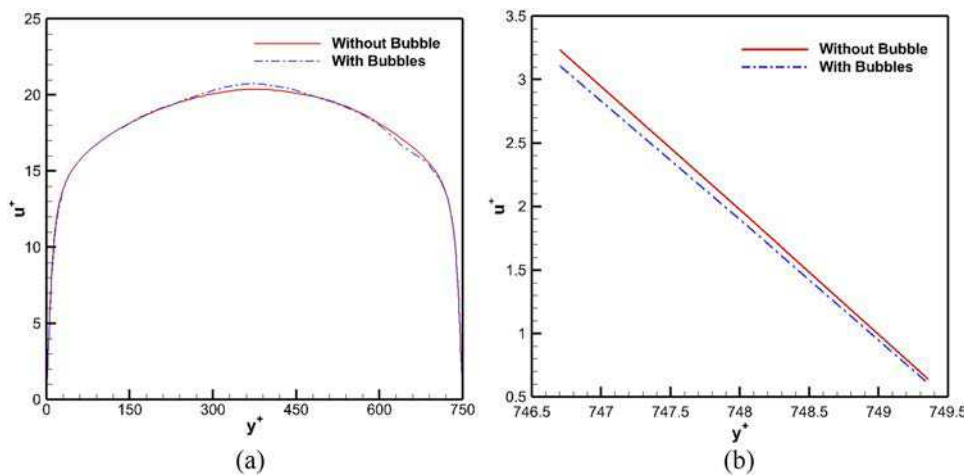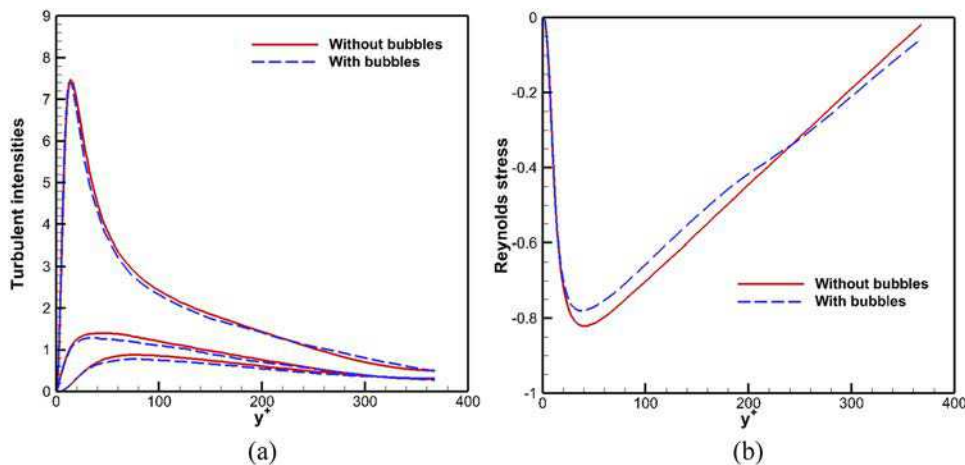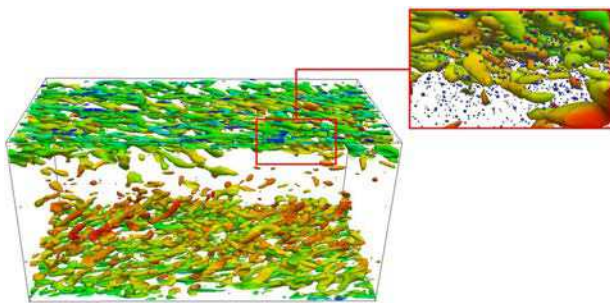

FIG. 10. Comparison of the mean liquid velocity profile with and without bubbles. (a) Velocity profile along the channel height. (b) Local velocity comparison near the upper wall.

FIG. 11. Comparison of turbulent intensities and Reynolds stress. (a) Turbulent intensities in three directions. (b) Reynolds stress.

FIG. 12. Instantaneous turbulent vortex structure field presented by the isosurfaces of Q.

V. TURBULENT BOUNDARY LAYER FLOW

In this section, bubbles are injected into a turbulent boundary layer flow to investigate the bubble migration and bubble-induced frictional drag reduction. Simulation parameters were chosen to match the experiment of Qin *et al.*[21] The drag reduction effect of the plate is calculated and compared with the experimental results. The migration movement of bubbles under turbulence and the corresponding effect on drag reduction are analyzed in detail.

A. Computational conditions

Mattson and Mahesh used a one-way coupled Euler–Lagrange-DNS method to study the migration of bubbles migration in a turbulent boundary layer before.[25] Because of the high computational cost of DNS methods, they carried out a scaled simulation based on Froude (Fr) number similarity. However, due to the complexity of bubble and boundary layer flows, it is difficult to achieve the consistency of the flow state by relying only on Fr number similarity. In this paper, by means of the LES method, numerical simulations with the same plate length, flow velocity, and gas flow rate with experiments are carried out. Parameters are chosen to match the experiment of Qin *et al.*[21] The length of the plate is 1.5 m, and the injector is placed at 0.123 m away from the leading edge in the

experiment. For the condition that the flow velocity is 4 m/s, the range of Reynolds numbers of the turbulent boundary layer is $1320 < Re_\theta < 9800$, using a power law to estimate boundary-layer momentum thickness.

The precursor channel flow simulation method[44] is adopted to generate the turbulent boundary layer inflow field. First, a fully developed turbulent channel flow is simulated using the same method as Sec. IV A, and the three-dimensional channel size and bulk velocity are set as the guidance provided by Mukha and Liefvendahl.[44] After the turbulent flow in the channel reaches stable, half of the inlet plane is taken as the sampling surface and the flow velocity is sampled at every time step. Next, a python package *eddylicious*[45] is used to convert the sampled data into the input format in the turbulent boundary layer simulation. The simulation of turbulent boundary layer flow is initialized from zero velocity and runs for a long time to ensure turbulence throughout the computational domain, and all transients are removed. The computational domain and fully developed turbulent boundary layer can be seen in Fig. 13.

The computational domain covers the whole length and 1/10 width of the flat plate in the experiment. In the wall-normal direction, the height of the computational domain is selected so that the boundary layer never occupies more than one-third of the domain. Specifically, in Fig. 11, $L = 1.377$ m, $B = 0.03$ m, and $H = 0.1$ m. The no-slip boundary condition is adopted for the top wall. The boundary of bubble injection is set at the front of the domain. Water and bubbles are free to exit at the outlet boundary. Three different gas flow rates are selected for simulation, $Q = 23.55$ l/min, $Q = 47.10$ l/min, and $Q = 58.88$ l/min. Most of the bubbles in the experiment maintain a diameter of 1 mm, so the number of bubbles injected per second can be calculated by the bubble flow rate and volume in the simulation. In the three cases, the injection rates of bubbles are 74 962/s, 149 924/s, and 187 421/s.

B. Drag reduction

The resistance of the upper plate is calculated after the bubble flow field reaches stability, and Fig. 14 shows the comparison of the drag reduction effect. The numerical simulation results
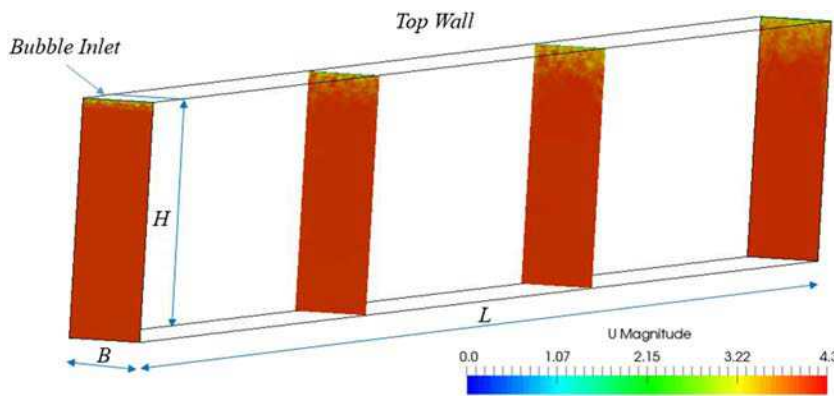
FIG. 13. Illustration of the computational domain and turbulent flow in the field.

represented by green circles in the figure are also from Qin *et al.*[21] They carried out an Euler–Euler simulation combined with the Reynolds Average Navier-Stokes (RANS) method to simulate the turbulent field. C_f and C_{f0} represent the frictional resistance coefficients with and without bubble injection. In general, the predicted trends of the two numerical results are in good concordance with experimental data. With the increase in gas flow rate, the drag reduction effect is further increased.

In terms of the specific magnitude of drag reduction, the numerical results obtained by using the Euler–Lagrange-LES method in this paper are more consistent with experimental results. The Euler–Euler-RANS results significantly underestimate the resistance. Qin *et al.*[21] points out that the reason for this underestimate comes from the influence of the spanwise marginal area of the plate, which is included in the experimental measurement but not taken into consideration in simulations. This is indeed a reason. In addition, we think that there are two reasons why the results of this paper are closer to the experiment. First, the
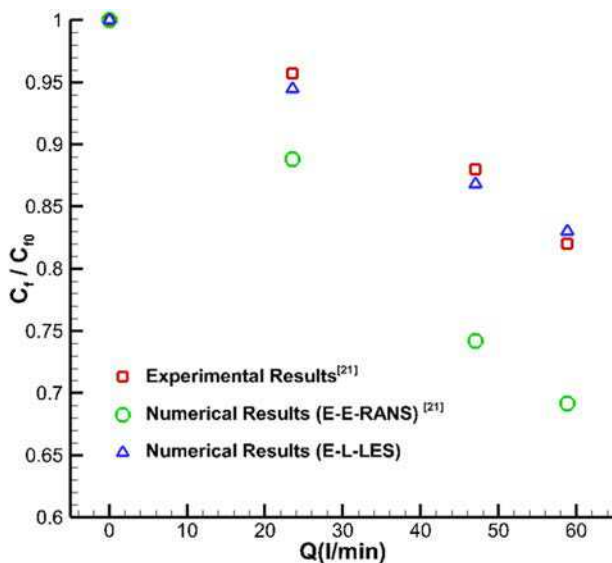
Euler–Lagrange method can more accurately simulate bubble motion and bubble–wall interaction. The motion and collision of bubbles near the wall have an influence on how well the bubbles adhere to the wall and further affect the drag reduction. Second, the turbulent flow simulation plays an important role for the bubble distribution. In this paper, a turbulent boundary layer is simulated by using the LES method as shown in Fig. 11. There are obvious fluctuations in the boundary layer, which leads to migration movement of bubbles. The flow field obtained by using the RANS method is smoother, resulting in more bubbles sticking to the plate, which leads to the over-predicted drag reduction effect. Trajectory and distribution of bubbles are further discussed in detail in Secs. V C–V F.

C. Distribution of bubbles and drag reduction effect

The bubble distribution is presented in Fig. 15. Bubbles are shown as blue spheres in the figure. As the flow develops downstream, migration movement of the bubbles away from the plate becomes more and more obvious. It can be seen in Fig. 13(b) that the bubbles have a significant velocity component in the wall-normal direction, which drives the bubbles away from the plate. This wall-normal velocity is due to the hydrodynamic force acting on bubbles.

Figure 16 shows the change in drag reduction effect along the length of the plate. Frictional resistance coefficient C_f/C_{f0} is plotted against the normalized streamwise distance x/L, where L represents the total length of the plate. The figure shows the averaged
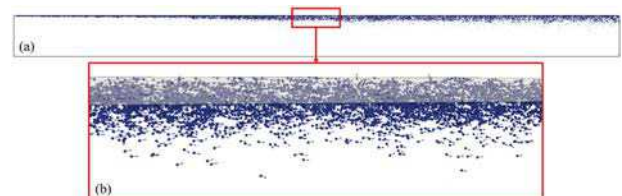

FIG. 14. Comparison of the drag reduction effect in different gas flow rates.

FIG. 15. Instantaneous bubble distribution in the turbulent boundary layer. (a) Overall view of bubble positions in streamwise and wall-normal coordinates. (b) 3-dimensional local view of bubbles with arrows indicating the direction of bubble velocity.
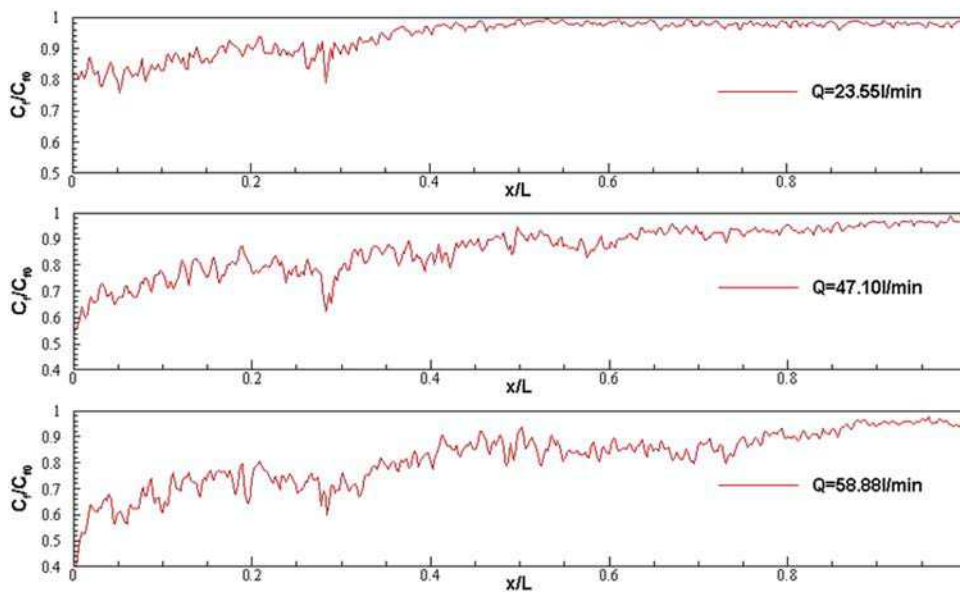
FIG. 16. Streamwise distribution of frictional resistance coefficients on the plate with three different air flow rates.

results in the spanwise direction. Under three different air flow rates, the distributions of the drag reduction effect follow the same rule, that is, the drag reduction effect decreases with the increase in the distance from the injector. Considering the bubble distribution shown in Fig. 15, it can be concluded that the effect of drag reduction depends almost entirely on the near-wall void fraction. In addition, it can be observed from Fig. 16 that the curve of the drag reduction effect has obvious oscillation. The local non-uniform distribution of the void fraction caused by the irregular movement of bubbles is the main reason for the oscillation. The migration movement of bubbles in the turbulent boundary layer is the main factor that determines the void fraction distribution. The effects of turbulence on bubble migration will be further discussed next.

D. The influence of turbulence

In order to verify the deterministic effects of turbulence on the bubble migration, a laminar boundary layer simulation with bubble injection is carried out. The computational domain and grid distribution remain the same with the turbulent boundary layer simulation as shown in Sec. V A. The liquid and bubble characteristics are matched between turbulent and laminar simulations at the liquid inlet and bubble injection boundary. Bubble distribution near the injector is shown in Fig. 17.

By the comparison of Figs. 15 and 17, the difference between bubble motion in turbulent and laminar boundary layers can be seen clearly. In the bubbly laminar boundary layer simulation, the

FIG. 17. Local view of bubble distribution near the injector in the laminar boundary layer.

bubbles are injected into the boundary layer with an initial velocity, so they travel a small distance. The initial velocity decays rapidly due to buoyancy and drag, and the bubbles travel toward the plate. Then, the bubbles collide with the plate and bounce back repeatedly within a certain range. Finally, the bubbles are in a state of balance between buoyancy and elastic forces in the wall-normal direction and move forward clinging to the plate.

Comparing the results of laminar and turbulent boundary layer simulations, it can be found that turbulence completely changes the behavior of bubbles. In turbulent flow, bubbles will gradually spread away from the plate, while in laminar flow, bubbles quickly attach to the plate and move forward. The underlying reason is that the bubbles are subjected to different liquid forces. In laminar flow, bubbles are almost in equilibrium with drag, buoyancy, and collision forces. Other forces are too small for the bubble to accelerate in the wall-normal direction. However, in the turbulent flow, the fluctuation characteristics of the turbulent boundary layer can significantly increase the effect of the fluid acceleration term Du/Dt on bubbles. Besides, the rotation of a bubble due to turbulence and the turbulent shear stress increases the lift force acting on the bubbles. Both the fluid acceleration and lift force can push the bubbles away from the wall.

E. The influence of different liquid forces

In order to study the effect of different liquid forces on the migration of bubbles, the averaged bubble trajectories are calculated with different source terms in the bubble kinematic equation. As shown in the right side of Eq. (6), the first term represents the drag effect, the second term represents the lift effect, and the third term represents the fluid acceleration effect. Three cases are set, of which case 1 only includes the drag term, case 2 includes the drag term and lift term, and case 3 includes the drag term, lift term, and fluid acceleration term. Buoyancy and collision forces are considered in
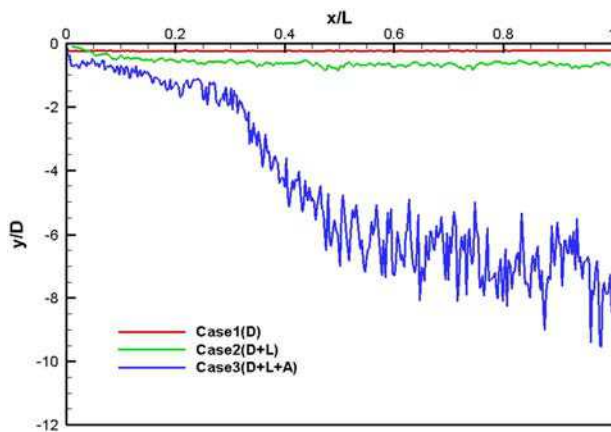
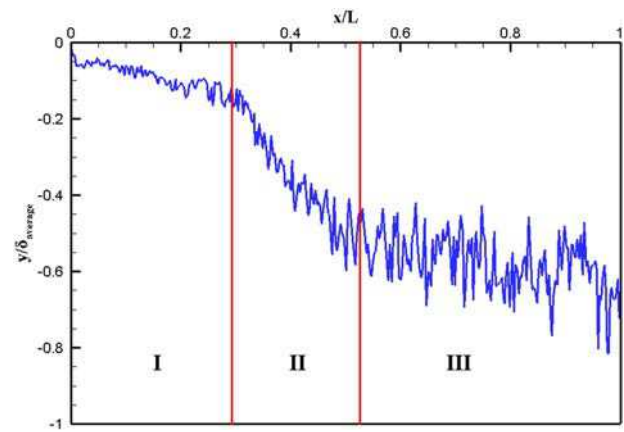**FIG. 18**. Averaged bubble trajectories with different liquid forces.

FIG. 19. Detailed analysis of three distinct stages of bubble trajectory.

all three cases. The averaged bubble trajectories between the three cases are shown in Fig. 18.

The coordinate origin in Fig. 18 is the position of the bubble injector. The displacement of the bubbles in the streamwise direction and wall-normal direction is nondimensionalized by the plate length and bubble diameter, respectively. The difference of bubble trajectories in the effect of the three forces can be seen clearly in Fig. 18. First, as it can be seen from the red line in the figure, drag does not cause the bubbles to migrate away from the plate. Under the effect of single drag force, bubbles remain attached to the plate along with small oscillations caused by the collision. When adding the lift force, the green line shows that the bubbles begin to migrate away from the plate and move with a nearly fixed small distance from the plate in the wall-normal direction. This proves that lift force does push the bubbles away from the plate, but the effect is not obvious. On this basis, when the fluid acceleration is considered, the bubble trajectory changes greatly as shown by the blue line. The bubbles migrate away from the plate obviously, and violent oscillation occurs in the downstream due to the turbulence. It can be concluded that the fluid acceleration is the most important reason for the migration of bubbles.

F. Three distinct stages of bubble trajectory

The averaged bubble trajectory considering all liquid forces is isolated for further analysis. The bubble movement can be clearly divided into three stages as shown in Fig. 19. The bubble displacement is nondimensionalized by the average boundary layer thickness on a plate $\delta_{average}$. In stage I, the bubbles are located in the inner layer of the turbulent boundary layer, where the flow velocity is relatively low and viscous force generated by the plate is dominant. Bubble velocity in the wall-normal direction changes slowly. A large number of bubbles cover the surface of the plate, separating the plate from the water. Due to the high void fraction, an excellent drag reduction effect can be obtained in this region. This phenomenon is called ALDR (Air-Layer Drag Reduction) in previous experiments.[11] Stage II is the transition state, the bubbles move significantly away from the plate due to the fluid acceleration of the turbulent flow. This is the main migration stage the bubbles move from the inner layer

of the turbulent boundary layer to the outer layer. In stage III, the tendency of bubble migration is reduced. Because of the continuous velocity fluctuation between the boundary layer and the main flow region, most of the bubbles oscillate in the outer layer of the boundary layer and keep a certain distance from the plate. Sanders observed a "liquid layer" between the downstream bubbles and the plate in experiments,[7] which is the same as stage III in our simulation. The low void fraction results in a poor drag reduction effect in this region.

VI. CONCLUSIONS

Bubble drag reduction in wall-bounded turbulent flows is investigated in detail with a two-way coupled Euler–Lagrange method. A nonlinear collision model suitable for bubble–bubble interaction and bubble–wall interaction is adopted. Two typical cases of wall-bounded turbulent flows, channel flow and turbulent boundary layer, are studied in this paper. For channel flow, bubbles are injected into the channel uniformly initially, while for the boundary layer, bubbles are injected through an inlet boundary with a constant air flow rate. The following conclusions can be obtained:

(1) A Gaussian distributed method for calculating the void fraction and interphase forces in the Euler grid is adopted for the two-way coupling process. This method is proved to be very effective in dealing with the bubble entering in the boundary layer, where the grid size may be smaller than the bubble diameter. When the diameter of a bubble is larger than the grid size, its volume is smoothed into the several grids it actually occupies. The accuracy and stability of the two-way coupling algorithm are improved obviously.

(2) The effect of bubbles on turbulent flow is studied in the channel flow cases. It is found that bubbles in space oscillate in the wall-normal direction near the plate and bubble stripes on the plate sway in the spanwise direction, resulting in the decrease in turbulent intensities. Moreover, the presence of a bubble cloud can reduce the Reynolds stress, which contributes to the turbulent drag reduction.

(3) To the best of our knowledge, it is the first endeavor to carry out bubble drag reduction simulation with the experimental setups using a two-way coupled Euler–Lagrange method. By adopting the appropriate bubble motion model, collision model, and the robust two-way coupled algorithm, the predicted drag reductions are in good agreement with experimental results.

(4) Drag reduction is found to be directly related to the migration of bubbles away from the wall. Turbulence is proved to be a decisive factor by comparison with the laminar flow simulation. For different liquid forces, drag force and buoyancy push bubbles toward the plate, while lift and fluid acceleration forces push bubbles away from the plate. Fluid acceleration force acting on bubble provides the dominate motivation for bubble migration.

(5) The bubble trajectory in the turbulent boundary layer can be divided into three stages. In the first stage, bubbles locate in the inner layer and the drag reduction effect is obvious. In the transition stage, bubbles accelerate away from the plate. Finally, the migration slows down while the oscillating motion is dominant, and bubbles are observed apart from the plate with lower drag reduction.

There are obvious fluid velocity fluctuation and strong shear stress in the turbulent boundary layer, which can lead to the deformation, breakup, and coalescence of bubbles. Bubbles will form a new size distribution after breakup and coalescence, which can affect the drag reduction effect. Future works will be focused on the development of new numerical methods to simulate the deformation, breakup, and coalescence of bubbles under strong turbulent shear stress in the boundary layer.

ACKNOWLEDGMENTS

REFERENCES

[1]K. Fukuda, J. Tokunaga, T. Nobunaga, T. Nakatani, and T. Iwasaki, "Frictional drag reduction with air lubricant over a super-water-repellent surface," J. Mar. Sci. Technol. **5**, 123–130 (2000).

[2]W. Abu, J. Hou, and S. Ghaemi, "Inner and outer layer turbulence over a super-hydrophobic surface with low roughness level at low Reynolds number," Phys. Fluids **29**(9), 095106 (2017).

[3]R. Costantini, J. P. Mollicone, and F. Battista, "Drag reduction induced by superhydrophobic surfaces in turbulent pipe flow," Phys. Fluids **30**(2), 025102 (2018).

[4]M. S. Naim and M. F. Baig, "Turbulent drag reduction in Taylor-Couette flows using different super-hydrophobic surface configurations," Phys. Fluids **31**, 095108 (2019).

[5]M. E. Mccormick and R. Bhattacharyya, "Drag reduction of a submersible hull by electrolysis," Nav. Eng. J. **85**(2), 11–16 (1973).

[6]N. K. Madavan, S. Detusch, and C. L. Merkle, "Reduction of turbulent skin-friction by microbubbles," Phys. Fluids **27**(2), 356–363 (1984).

[7]N. K. Madavan, S. Detusch, and C. L. Merkle, "Measurements of local skin friction in a microbubble modified turbulent boundary layer," J. Fluid Mech. **156**, 237–256 (1985).

[8]S. Pal, C. L. Merkle, and S. Deutsch, "Bubble characteristics and trajectories in a microbubble boundary layer," Phys. Fluids **31**(4), 744–751 (1988).

[9]E. S. Winkel, S. L. Ceccio, D. R. Dowling, and M. Perlin, "Bubble-size distributions produced by wall injection of air into flowing freshwater, saltwater and surfactant solutions," Exp. Fluids **37**, 802–810 (2004).

[10]W. C. Sanders, E. S. Winkel, D. R. Dowling, M. Perlin, and S. L. Ceccio, "Bubble friction drag reduction in a high-Reynolds-number flat-plate turbulent boundary layer," J. Fluid Mech. **552**, 353–380 (2006).

[11]B. R. Elbing, E. S. Winkel, K. A. Lay, S. L. Ceccio, D. R. Dowling, and M. Perlin, "Bubble-induced skin-friction drag reduction and the abrupt transition to air-layer drag reduction," J. Fluid Mech. **612**, 201–236 (2008).

[12]B. Jacob, A. Olivieri, M. Miozzi et al., "Drag reduction by microbubbles in a turbulent boundary layer," Phys. Fluids **22**(11), 115104 (2010).

[13]S. Hassan and N. Morteza, "Determination of optimum injection flow rate to achieve maximum micro bubble drag reduction in ships: An experimental approach," Sci. Iran. B **20**(3), 535–541 (2013).

[14]H. J. Park, Y. Tasaka et al., "Drag reduction promoted by repetitive bubble injection in turbulent channel flows," Int. J. Multiphase Flow **75**, 12–25 (2015).

[15]H. J. Park, Y. Tasaka et al., "Bubbly drag reduction accompanied by void wave generation inside turbulent boundary layers," Exp. Fluids **59**, 166 (2018).

[16]Y. Jiang, S. W. Jeong et al., "Experimental investigation of drag characteristics of ventilated supercavitating vehicles with different body shapes," Phys. Fluids **31**, 052106 (2019).

[17]R. F. Kunz, S. Deutsch, and J. W. Lindau, "Two fluid modeling of microbubble turbulent drag reduction," in Proceedings of the 4TH ASME-JSME Joint Fluids Engineering Conference, FEDSM'03 (ASME, Honolulu, Hawaii, 2003), Paper No. FED2003-45640.

[18]R. F. Kunz, H. J. Gibeling, M. R. Maxey, G. Tryggvason, A. A. Fontaine, H. L. Petrie, and S. L. Ceccio, "Validation of two-fluid Eulerian CFD modelling for microbubble drag reduction across a wide range of Reynolds numbers," J. Fluids Eng. **129**, 66–79 (2007).

[19]K. Mohanarangam, S. C. P. Cheung, J. Y. Tu et al., "Numerical simulation of micro-bubble drag reduction using population balance model," Ocean Eng. **36**(11), 863–872 (2009).

[20]M. Xiang, S. C. P. Cheung, J. Y. Tu et al., "Numerical research on drag reduction by ventilated partial cavity based on two-fluid model," Ocean Eng. **38**(17-18), 2023–2032 (2011).

[21]S. Qin, N. Chu, Y. Yao et al., "Stream-wise distribution of skin-friction drag reduction on a flat plate with bubble injection," Phys. Fluids **29**, 037103 (2017).

[22]D. Lakehal, D. Metrailler, and S. Reboux, "Turbulent water flow in a channel at Re$_\tau$ = 400 laden with 0.25 mm diameter air-bubbles clustered near the wall," Phys. Fluids **29**(6), 065101 (2017).

[23]J. Xu, M. R. Maxey, and G. E. Karniadakis, "Numerical simulation of turbulent drag reduction using micro-bubbles," J. Fluid Mech. **468**, 271–281 (2002).

[24]A. Ferrante and S. Elghobashi, "On the physical mechanisms of drag reduction in a spatially developing turbulent boundary layer laden with microbubbles," J. Fluid Mech. **503**, 345–355 (2004).

[25]M. Mattson and K. Mahesh, "Simulation of bubble migration in a turbulent boundary layer," Phys. Fluids **23**(4), 045107 (2011).

[26]M. Pang, J. Wei, B. Yu et al., "Numerical investigation on turbulence and bubbles distribution in bubbly flow under normal gravity and microgravity conditions," Microgravity Sci. Technol. **22**(3), 283–294 (2010).

[27]D. Molin, C. Marchioli, and A. Soldati, "Turbulence modulation and microbubble dynamics in vertical channel flow," Int. J. Multiphase Flow **42**, 80–95 (2012).

[28]M. Pang, J. Wei, and B. Yu, "Numerical study on modulation of microbubbles on turbulence frictional drag in a horizontal channel," Ocean Eng. **81**, 58–68 (2014).

[29]K. S. Asiagbe, M. Fairweather, D. O. Njobuenwu, and M. Colombo, "Large eddy simulation of microbubble transport in a turbulent horizontal channel flow," Int. J. Multiphase Flow **94**, 80–93 (2017).

[30]F. Nicoud and F. Ducros, "Subgrid-scale stress modelling based on the square of the velocity gradient tensor flow," Turbul. Combust. **62**, 183–200 (1999).

[31]A. Tomiyama, G. P. Celata, S. Hosokawa, and S. Yoshida, "Terminal velocity of single bubbles in surface tension force dominant regime," Int. J. Multiphase Flow **28**, 1497–1519 (2002).

[32]A. Tomiyama, H. Tamai, I. Zun, and S. Hosokawa, "Transverse migration of single bubbles in simple shear flows," Chem. Eng. Sci. **57**, 1849–1858 (2002).

[33]C. Zhang, J. Li, L. Luo et al., "Numerical simulation for a rising bubble interacting with a solid wall: Impact, bounce, and thin film dynamics," Phys. Fluids **30**(11), 112106 (2018).

[34]S. Heitkam, A. E. Sommer, W. Drenckhan et al., "A simple collision model for small bubbles," J. Phys.: Condens. Matter **29**(12), 124005 (2017).

[35]J. Ma, G. L. Chahine, and C. T. Hsiao, "Spherical bubble dynamics in a bubbly medium using an Euler-Lagrange model," Chem. Eng. Sci. **128**, 64–81 (2015).

[36]R. Raju, S. Singh, C.-T. Hsiao, and G. Chahine, "Study of pressure wave propagation in a two-phase bubbly mixture," J. Fluid Eng. **133**(12), 121302 (2011).

[37]J. Capecelatro and O. Desjardins, "An Euler-Lagrange strategy for simulating particle-laden flows," J. Comput. Phys. **238**, 1–31 (2013).

[38]P. C. Duineveld, "The rise velocity and shape of bubbles in pure water at high Reynolds number," J. Fluid Mech. **292**, 325–332 (1995).

[39]R. D. Moser, J. Kim, and N. N. Mansour, "Direct numerical simulation of turbulent channel flow up to $Re_\tau = 590$," Phys. Fluids **11**(4), 943–945 (1999).

[40]M. R. Head and P. Bandyopadhyay, "New aspects of turbulent boundary-layer structure," J. Fluid Mech. **107**(1), 297 (1981).

[41]M. Marchis and B. Milici, "Turbulence modulation by micro-particles in smooth and rough channels," Phys. Fluids **28**(11), 115101 (2016).

[42]K. Luo, C. Hu, F. Wu et al., "Direct numerical simulation of turbulent boundary layer with fully resolved particles at low volume fraction," Phys. Fluids **29**(5), 053301 (2017).

[43]K. Fukagata, K. Iwamoto, and N. Kasagi, "Contribution of Reynolds stress distribution to the skin friction in wall-bounded flows," Phys. Fluids **14**(11), L73–L76 (2002).

[44]T. Mukha and M. Liefvendahl, "The generation of turbulent inflow boundary conditions using precursor channel flow simulations," Comput. Fluids **156**, 21–33 (2017).

[45]T. Mukha and M. Liefvendahl, "Eddylicious: A Python package for turbulent inflow generation," SoftwareX **7**, 112–114 (2018).